Advances in Engineering Software 131 (2019) 217–231

Contents lists available at ScienceDirect

Advances in Engineering Software

journal homepage: www.elsevier.com/locate/advengsoft

On structural topology optimization considering material nonlinearity: Plane strain versus plane stress solutions

Heng Chi[a], Davi L. Ramos[b], Adeildo S. Ramos Jr.[b], Glaucio H. Paulino[*,a]

[a] School of Civil and Environmental Engineering, Georgia Institute of Technology, 790 Atlantic Drive, Atlanta, GA 30332-0355, USA
[b] Federal University of Alagoas, Maceio, AL, Brazil

ARTICLE INFO

Keywords:
Topology optimization
Material nonlinearity
Plane stress
Plane strain
Ogden-based model

ABSTRACT

We present a structural topology optimization framework considering material nonlinearity by means of a tailored hyperelastic formulation. The nonlinearity is incorporated through a hyperelastic constitutive model, which is capable of capturing a range of nonlinear material behavior under both plane strain and plane stress conditions. We explore both standard (i.e. quadrilateral) and polygonal finite elements in the solution process, and achieve smooth convergence in both the optimization process and the solution of nonlinear state equations. Numerical examples are presented, which demonstrate that the topology optimization framework can effectively capture the influence of various material behaviors, load levels and loading conditions (i.e. plane stress versus plane strain) on the optimal topologies.

1. Introduction

The field of topology optimization considering nonlinear structural problems is vibrant and growing. In topology optimization of nonlinear structural problems, one can find different optimal topologies from those that are obtained only considering linear material behavior, reflecting the influence of nonlinearity on the performance of structure. In the literature, most work focuses on problems of elastic material under finite displacement or strain, which introduce challenges in solving the nonlinear state equations due to global and local instabilities and excessive distortion of low-density elements. To overcome these challenges, various techniques have been proposed in the literature. For instance, to avoid the influence of low density elements on the convergence of nonlinear structural analysis, Buhl et al. [15] propose to relax the convergence criterion of the Newton-Raphson method at the nodes surrounded by low-density elements. From another perspective, Kawamoto [27] proposes to replace the Newton–Raphson method with the Levenberg–Marguardt method and demonstrates its effectiveness in alleviating the numerical difficulties in solving the nonlinear structure equations. Yoon and Kim [50] adopt an element connectivity parametrization scheme to overcome the numerical instability of low density elements, in which the structural topology is parametrized by a set of zero length elastic links. Instead of optimizing the density of the finite element, they optimize the density of the links (which relates to the stiffness of the link). Wang et al. [48] propose an interpolation scheme to stabilize numerical instability of low density elements, which interpolates between the true stored-energy function and the stored-energy function of linear elasticity based on element densities. As a result, they use the true stored-energy function for solid elements and the stored-energy function of linear elasticity for low density elements. In addition, Van Dijk et al. [46] introduce a deformation scaling technique to scale down the deformation of the low density elements and Luo et al. [32] develop an additive hyperelastic technique that is able to alleviate excessive deformation and instability of low-density elements. For material nonlinearity, on the other hand, the topology optimization literature typically considers non-tension/non-compression [14,16,24,36], bilinear materials [17,22,31] in the continuum setting and asymmetric tension and compression stress limit [1] or tension and compression stiffness [52] in the truss layout optimization. In addition, we also mention the work by Pedersen [35], in which a power-law material model is studied, and the work by Taylor and co-authors [43–45], in which piecewise-linear material models capable of controlling strain hardening/softening levels are considered. More general nonlinear material models, which can capture not only the influence of tension/compression asymmetry but also that of different load levels on the layout of optimal designs, however, are rarely considered. For instance, when a non-tension/non-compression or bilinear material is considered, because the moduli in both tension and compression are constants, the influence of varying load level on the layout of optimized designs may not be fully captured.

* Corresponding author.
E-mail address: paulino@gatech.edu (G.H. Paulino).

https://doi.org/10.1016/j.advengsoft.2018.08.017
Received 22 March 2018; Received in revised form 5 August 2018; Accepted 30 August 2018
Available online 01 March 2019
0965-9978/

Nomenclature

$\boldsymbol{\varepsilon}$	Linearized strain tensor
$\boldsymbol{\sigma}$	Cauchy stress tensor
$\boldsymbol{C}$	Tangent modulus tensor
$\bar{\varepsilon}_\alpha$	The αth principal strain
$\boldsymbol{n}_\alpha$	Principal direction (eigenvector) associated with $\bar{\varepsilon}_\alpha$
$\bar{\sigma}_\alpha$	The αth principal stress
Ψ	Stored energy function in terms of principal strains
λ_α	The αth principal stretch
α_q	Material parameter in the Ogden-based model
β_q	Material parameter in the Ogden-based model
η_q	Material parameter in the Ogden-based model
N_O	Material parameter in the Ogden-based model
λ, μ	Lame's constants
$\boldsymbol{D}$	Matrix representation of $\boldsymbol{C}$
$\boldsymbol{\sigma}$	Stress vector $\underline{\boldsymbol{\sigma}} = [\sigma_{11}, \sigma_{22}, \sigma_{12}]^T$
$\boldsymbol{\varepsilon}$	Strain vector $\underline{\boldsymbol{\varepsilon}} = [\varepsilon_{11}, \varepsilon_{22}, \gamma_{12}]^T$
γ_{12}	Shear strain
Ω_h	A discretization of the domain Ω
Γ_h^t	The boundary of the mesh where traction is applied
Γ_h^x	The boundary of the mesh where displacement is applied
$\mathcal{K}_h$	Discrete global displacement space
E	A generic element of the mesh Ω_h
E_0	Young's modulus
ν	Poisson's ratio
∇	Gradient operator
Π_h	Potential energy of the discretization
$\boldsymbol{U}$	Global nodal displacement vector
$\boldsymbol{R}$	Global residual vector
$\boldsymbol{F}_{int}$	Global internal force vector
$\boldsymbol{F}_{ext}$	Global external force vector
$\boldsymbol{K}$	Global tangent stiffness matrix
$\boldsymbol{U}^{(k)}$	Global nodal displacement vector at kth Newton's iteration
$\xi^{(k)}$	Step size at kth Newton's iteration
τ	Parameter in the line search algorithm
κ	Step size reduction parameter in the line search algorithm
f	Objective function of topology optimization
g	Volume constraint function of topology optimization
$\boldsymbol{A}$	Element area vector
ρ	The vector of design variables
ρ_e	The design variable of the eth element
$\tilde{\boldsymbol{\rho}}$	The filtered vector of design variables
$\tilde{\rho}_e$	The filtered design variable of the eth element
$\boldsymbol{P}$	Density filter matrix
$V_{\max}$	Maximum allowable volume fraction
η	Damping ratio of the OC update
$move$	Move limit of the OC update

In the work of Ramos Jr. and Paulino [37], a topology optimization formulation considering a general hyperelastic material model under small deformation is proposed for truss layout optimization using the ground structure method. This optimization formulation is proven to be convex provided that the tangent stiffness matrix is positive definite, is free of issues related to global and local instabilities, and is able to capture the influence of both material behavior and load level on the layout of the optimal structures. More recently, this optimization formulation was extended to incorporate a discrete filter to improve the computational efficiency [52] and to address multi-material topology optimization [51].

In this work, we present a continuum topology optimization framework considering a general hyperelastic material model under small deformation derived from the Ogden model [33]. Both plane strain and plane stress conditions are addressed. Unlike the work by Pedersen [35], which adopts power law nonlinear elastic models with strain softening behavior, our constitutive model is flexible in controlling tension-compression asymmetry and exhibits strain hardening responses (i.e. no limit points in the stress-strain relationship), which allows us to confidently utilize a load control strategy in solving the nonlinear state equations. To efficiently solve the resulting nonlinear state equation, we introduce the Armijo-type inexact line search scheme to the standard Newton's method, which significantly improves convergence performance.

Another issue in topology optimization considering nonlinear structural problems is the actual definition of the objective function. In contrast to the case when linear material behavior is assumed, various types of objective functions exist for nonlinear optimization problems, see, e.g., [15,28,30,37,39]. In this work, we choose the objective function
as the total potential energy function at the equilibrium state (see, e.g. [37]). This objective is also adopted and studied in references [25,29,30,37,52]. The advantages of this objective function are that there is no need to compute the adjoint vector in the sensitivity analysis, and its sensitivity is guaranteed to be non-positive.

The remainder of the paper is organized as follows. Section 2 puts forth the hyperelastic constitutive model under small strain and specializes it to two-dimensional plane strain and plane stress conditions. Section 3 reviews the nonlinear finite element analysis and introduces the Armijo-type inexact line search scheme. In Section 4, we present the topology optimization formulation proposed in this work and address its corresponding sensitivity analysis. In Section 5, four representative numerical examples are presented to showcase the effectiveness and robustness of the proposed topology optimization framework. Section 6 contains several concluding remarks. In summary, this research systematically outlines an effective topology optimization framework for continuum structures considering material nonlinearity only.

2. Hyperelastic constitutive model under small deformation

Hyperelastic material models in the literature are typically for finite deformations. In this section, we introduce an isotropic hyperelastic model that accommodates the small deformation assumption based on the Ogden model [33]. Under small deformation, the linearized strain tensor $\boldsymbol{\varepsilon}$ is given by

$$\boldsymbol{\varepsilon} = \frac{1}{2}[\nabla \boldsymbol{u} + (\nabla \boldsymbol{u})^T], \tag{1}$$

where $\boldsymbol{u}$ is the displacement field and ∇ stands for the gradient operator.

The strain tensor can be alternatively expressed in terms of its principal strains $\bar{\varepsilon}_\alpha$ using the spectral representation [11,34]

$$\boldsymbol{\varepsilon} = \sum_{\alpha=1}^{3} \bar{\varepsilon}_\alpha \boldsymbol{n}_\alpha \otimes \boldsymbol{n}_\alpha, \tag{2}$$

where $\boldsymbol{n}_\alpha$ is the principal direction (eigenvector) associated with $\bar{\varepsilon}_\alpha$ and $\otimes$ denotes the usual tensor product. For isotropic hyperelastic solids, the stored-energy Ψ is a function of $\bar{\varepsilon}_\alpha$, i.e. $\Psi(\bar{\varepsilon}_1, \bar{\varepsilon}_2, \bar{\varepsilon}_3)$. The stress and strain tensors are coaxial for isotropic solids [34], meaning that the following spectral representation holds

$$\boldsymbol{\sigma} = \sum_{\alpha=1}^{3} \bar{\sigma}_\alpha \boldsymbol{n}_\alpha \otimes \boldsymbol{n}_\alpha, \quad \bar{\sigma}_\alpha = \frac{\partial \Psi}{\partial \bar{\varepsilon}_\alpha}(\bar{\varepsilon}_1, \bar{\varepsilon}_2, \bar{\varepsilon}_3), \quad \alpha = 1, \ldots, 3 \tag{3}$$

where $\bar{\sigma}_\alpha$ are the principal stresses.

Similarly, the tangent modulus tensor $\boldsymbol{C}$ can also be expressed in the following spectral representation [11]:

$$\begin{aligned}\boldsymbol{C} &= \sum_{\alpha=1}^{3}\sum_{\beta=1}^{3}\frac{\partial\bar{\sigma}_\alpha}{\partial\bar{\varepsilon}_\beta}\boldsymbol{n}_\alpha\otimes\boldsymbol{n}_\alpha\otimes\boldsymbol{n}_\beta\otimes\boldsymbol{n}_\beta \\ &+ \sum_{\alpha=1}^{3}\sum_{\beta=1,\beta\neq\alpha}^{3}\frac{1}{2}\left(\frac{\bar{\sigma}_\alpha-\bar{\sigma}_\beta}{\bar{\varepsilon}_\alpha-\bar{\varepsilon}_\beta}\right)(\boldsymbol{n}_\alpha\otimes\boldsymbol{n}_\beta\otimes\boldsymbol{n}_\alpha\otimes\boldsymbol{n}_\beta \\ &+ \boldsymbol{n}_\alpha\otimes\boldsymbol{n}_\beta\otimes\boldsymbol{n}_\beta\otimes\boldsymbol{n}_\alpha).\end{aligned} \tag{4}$$

We note that the coefficients of the second term on the right hand side of the above expression become singular when $\bar{\varepsilon}_\alpha$ and $\bar{\varepsilon}_\beta$ are identical. In such cases, these coefficients should be replaced by their limits [11]

$$\lim_{\bar{\varepsilon}_\beta\to\bar{\varepsilon}_\alpha}\frac{\bar{\sigma}_\alpha-\bar{\sigma}_\beta}{\bar{\varepsilon}_\alpha-\bar{\varepsilon}_\beta}=\frac{\partial\bar{\sigma}_\beta}{\partial\bar{\varepsilon}_\beta}-\frac{\partial\bar{\sigma}_\alpha}{\partial\bar{\varepsilon}_\beta}. \tag{5}$$

2.1. Ogden-based material model

The stored-energy function utilized in this work is derived from the compressible Ogden model provided in references [23,33]

$$\begin{aligned}\Psi(\bar{\varepsilon}_1,\bar{\varepsilon}_2,\bar{\varepsilon}_3) &= \sum_{q=1}^{N_O}\frac{\eta_q}{\alpha_q}(\lambda_1^{\alpha_q}+\lambda_2^{\alpha_q}+\lambda_3^{\alpha_q}-3) \\ &+ \sum_{q=1}^{N_O}\frac{\eta_q}{\alpha_q\beta_q}\left[(\lambda_1\lambda_2\lambda_3)^{-\alpha_q\beta_q}-1\right],\end{aligned} \tag{6}$$

where α_q, β_q, η_q and N_O are material parameters; and $\lambda_\alpha \doteq \bar{\varepsilon}_\alpha + 1$, $\alpha = 1, 2, 3$, are the principal stretches under small deformation. According to Eq. (3), the specific form of the principal stresses for this Ogden-based material is expressed as

$$\bar{\sigma}_\alpha(\bar{\varepsilon}_1,\bar{\varepsilon}_2,\bar{\varepsilon}_3)=\sum_{q=1}^{N_O}\eta_q\left[(1+\bar{\varepsilon}_\alpha)^{\alpha_q-1}-(1+\bar{\varepsilon}_\alpha)^{-1}J^{-\alpha_q\beta_q}\right], \tag{7}$$

where $J \doteq (1+\bar{\varepsilon}_1)(1+\bar{\varepsilon}_2)(1+\bar{\varepsilon}_3)$. In addition, the coefficients in the tangent modulus tensor of the Ogden-based material is given by

$$\frac{\partial\bar{\sigma}_\alpha}{\partial\bar{\varepsilon}_\beta}=\begin{cases}\displaystyle\sum_{q=1}^{N_O}\eta_q(\alpha_q-1)(\bar{\varepsilon}_\alpha+1)^{\alpha_q-2} \\ \quad+(1+\bar{\varepsilon}_\alpha)^{-2}\eta_q(1+\alpha_q\beta_q)J^{-\alpha_q\beta_q}, & \alpha=\beta \\ \displaystyle\sum_{q=1}^{N_O}(1+\bar{\varepsilon}_\alpha)^{-1}(1+\bar{\varepsilon}_\beta)^{-1}\eta_q\alpha_q\beta_qJ^{-\alpha_q\beta_q}, & \alpha\neq\beta\end{cases} \tag{8}$$

For consistency with the linear elasticity theory, the above derived constitutive model must satisfy the following three conditions in the undeformed state ($\bar{\varepsilon}_\alpha = 0, \alpha = 1, 2, 3$): (i) $\Psi = 0$; (ii) $\bar{\sigma}_\alpha = 0, \alpha = 1, 2, 3$; and (iii) $C_{ijkl} = \lambda\delta_{ij}\delta_{kl} + \mu(\delta_{ik}\delta_{jl} + \delta_{il}\delta_{jk})$ where λ and μ are the Lamé constants. Based on Eqs. (6) and (7), conditions (i) and (ii) are satisfied by definition. By comparing condition (iii) with the tangent modulus tensor given in Eq. (4), we obtain the following relations between the set of material parameters in the Ogden-based material and the Lamé constants:

$$\lambda=\sum_{q=1}^{N_O}\eta_q\alpha_q\beta_q \quad\text{and}\quad \mu=\frac{1}{2}\sum_{q=1}^{N_O}\eta_q\alpha_q. \tag{9}$$

2.2. Ogden-based model under plane strain conditions

In the subsequent subsections, we simplify the Ogden-based constitutive model under plane strain and plane stress conditions. For both conditions, we assume that the principal strain $\bar{\varepsilon}_3$ is in the out-of-plane direction. The associated principal stress $\bar{\sigma}_3$ is thus decoupled from the problem. For better connection with the finite element (FE) implementation, we adopt the matrix-vector notation (the Voigt notation) [11]. We define the stress and strain vectors as $\underline{\boldsymbol{\sigma}} = [\sigma_{11}, \sigma_{22}, \sigma_{12}]^T$ and $\underline{\boldsymbol{\varepsilon}} = [\varepsilon_{11}, \varepsilon_{22}, \gamma_{12}]^T$, where $\gamma_{12} = \varepsilon_{12} + \varepsilon_{21}$ is the shear strain. The tangent modulus matrix $\boldsymbol{D}$ takes the usual form:

$$\boldsymbol{D}=\begin{bmatrix}C_{1111} & C_{1122} & C_{1112}\\ & C_{2222} & C_{2212}\\ \text{sym.} & & C_{1212}\end{bmatrix}. \tag{10}$$

2.2.1. Ogden-based model under plane strain condition

Under the plane strain condition, $\bar{\varepsilon}_3 = 0$ and $\bar{\sigma}_3$ is decoupled from the problem. We can express the in-plane principal strains (assuming $\bar{\varepsilon}_1 \geq \bar{\varepsilon}_2$ without loss of generality) at a general strain state $\boldsymbol{\varepsilon}$ as [7]

$$\begin{aligned}\bar{\varepsilon}_1 &= \frac{\varepsilon_{11}+\varepsilon_{22}}{2}+\sqrt{\left(\frac{\varepsilon_{11}-\varepsilon_{22}}{2}\right)^2+\left(\frac{\gamma_{12}}{2}\right)^2}, \\ \bar{\varepsilon}_2 &= \frac{\varepsilon_{11}+\varepsilon_{22}}{2}-\sqrt{\left(\frac{\varepsilon_{11}-\varepsilon_{22}}{2}\right)^2+\left(\frac{\gamma_{12}}{2}\right)^2}.\end{aligned} \tag{11}$$

Their associated principal directions are given by $\boldsymbol{n}_1 = [\cos(\theta), \sin(\theta)]^T$ and $\boldsymbol{n}_2 = [-\sin(\theta), \cos(\theta)]^T$ where θ is the angle between the principal direction $\boldsymbol{n}_1$ and the basis vector $\boldsymbol{e}_1$ in the Cartesian frame of reference. The in-plane principal stresses are evaluated based on Eq. (7) as $\bar{\sigma}_\alpha(\bar{\varepsilon}_1, \bar{\varepsilon}_2, 0)$, $\alpha = 1, 2$.

Based on relation (3), the transformation between the principal stress and stress vector $\boldsymbol{\sigma}$ can be expressed as

$$\underline{\boldsymbol{\sigma}}=\boldsymbol{T}^T\begin{bmatrix}\bar{\sigma}_1(\bar{\varepsilon}_1,\bar{\varepsilon}_2,0)\\ \bar{\sigma}_2(\bar{\varepsilon}_1,\bar{\varepsilon}_2,0)\end{bmatrix}, \tag{12}$$

where the transformation matrix $\boldsymbol{T}$ is given by

$$\boldsymbol{T}=\begin{bmatrix}(\cos(\theta))^2 & (\sin(\theta))^2 & \sin(2\theta)/2\\ (\sin(\theta))^2 & (\cos(\theta))^2 & -\sin(2\theta)/2\end{bmatrix}. \tag{13}$$

In addition, when $\bar{\varepsilon}_1 > \bar{\varepsilon}_2$, the tangent modulus matrix $\boldsymbol{D}$ is given by

$$\begin{aligned}\boldsymbol{D} &= \boldsymbol{T}^T\begin{bmatrix}\partial\bar{\sigma}_1(\bar{\varepsilon}_1,\bar{\varepsilon}_2,0)/\partial\bar{\varepsilon}_1 & \partial\bar{\sigma}_1(\bar{\varepsilon}_1,\bar{\varepsilon}_2,0)/\partial\bar{\varepsilon}_2\\ \partial\bar{\sigma}_2(\bar{\varepsilon}_1,\bar{\varepsilon}_2,0)/\partial\bar{\varepsilon}_1 & \partial\bar{\sigma}_2(\bar{\varepsilon}_1,\bar{\varepsilon}_2,0)/\partial\bar{\varepsilon}_2\end{bmatrix}\boldsymbol{T} \\ &+ \frac{\bar{\sigma}_1(\bar{\varepsilon}_1,\bar{\varepsilon}_2,0)-\bar{\sigma}_2(\bar{\varepsilon}_1,\bar{\varepsilon}_2,0)}{4(\bar{\varepsilon}_1-\bar{\varepsilon}_2)}\begin{bmatrix}1-\cos(4\theta) & \cos(4\theta)-1 & -\sin(4\theta)\\ & 1-\cos(4\theta) & \sin(4\theta)\\ \text{sym.} & & \cos(4\theta)+1\end{bmatrix}.\end{aligned} \tag{14}$$

When $\bar{\varepsilon}_1 = \bar{\varepsilon}_2$, the two principal directions $\boldsymbol{n}_1$ and $\boldsymbol{n}_2$ are not unique. In fact, any pair of orthogonal unit vectors can be considered principal directions in this case. Moreover, the above expression for **D** will not hold because its second term will become singular. In this case, the tangent modulus matrix $\boldsymbol{D}$ can be evaluated by taking the limit of the second term when $\bar{\varepsilon}_1 \to \bar{\varepsilon}_2$ and assuming a simple choice of principal directions, namely $\boldsymbol{n}_1 = [1, 0]^T$ and $\boldsymbol{n}_2 = [0, 1]^T$ (corresponding to $\theta = 0$). Based on (5), we have that

$$\boldsymbol{D}=\begin{bmatrix}\partial\bar{\sigma}_1(\bar{\varepsilon}_1,\bar{\varepsilon}_2,0)/\partial\bar{\varepsilon}_1 & \partial\bar{\sigma}_1(\bar{\varepsilon}_1,\bar{\varepsilon}_2,0)/\partial\bar{\varepsilon}_2 & 0\\ \partial\bar{\sigma}_2(\bar{\varepsilon}_1,\bar{\varepsilon}_2,0)/\partial\bar{\varepsilon}_1 & \partial\bar{\sigma}_2(\bar{\varepsilon}_1,\bar{\varepsilon}_2,0)/\partial\bar{\varepsilon}_2 & 0\\ 0 & 0 & \frac{1}{2}[\partial\bar{\sigma}_1(\bar{\varepsilon}_1,\bar{\varepsilon}_2,0)/\partial\bar{\varepsilon}_1 \\ & & -\partial\bar{\sigma}_1(\bar{\varepsilon}_1,\bar{\varepsilon}_2,0)/\partial\bar{\varepsilon}_2]\end{bmatrix}. \tag{15}$$

Moreover, in the limit of strain state $\underline{\boldsymbol{\varepsilon}}$ goes to $\boldsymbol{0}$, $\boldsymbol{D}$ reduces to the standard material modulus for linear elasticity under plane strain condition [20].

2.2.2. Ogden-based model under plane stress condition

Under plane stress condition, the principal strain $\bar{\varepsilon}_3$ is non-zero, but the corresponding principal stress $\bar{\sigma}_3$ is 0. This yields the following

nonlinear equation to solve the out of plane principal strain $\bar{\varepsilon}_3$:

$$\sum_{q=1}^{N_O} \eta_q \left[(1+\bar{\varepsilon}_3)^{\alpha_q - 1} - (1+\bar{\varepsilon}_3)^{-1} J^{-\alpha_q \beta_q} \right] = 0, \tag{16}$$

where $\bar{\varepsilon}_1$ and $\bar{\varepsilon}_2$ (again, assuming $\bar{\varepsilon}_1 \geq \bar{\varepsilon}_2$) are the in-plane principal strains. Denoting the solution to the above nonlinear equation as $\bar{\varepsilon}_3^*(\bar{\varepsilon}_1, \bar{\varepsilon}_2)$, the in-plane principal stresses are computed as $\bar{\sigma}_\alpha(\bar{\varepsilon}_1, \bar{\varepsilon}_2, \bar{\varepsilon}_3^*)$, $\alpha = 1, 2$ according to Eq. (7). The stress vector $\boldsymbol{\sigma}$ is then computed using the principal stresses and the same transformation given in Eq. (12).

When $\bar{\varepsilon}_1 > \bar{\varepsilon}_2$, the tangent modulus matrix $\boldsymbol{D}$ can be obtained as follows

$$\begin{aligned} \boldsymbol{D} = \boldsymbol{T} \left(\begin{bmatrix} \partial\bar{\sigma}_1/\partial\bar{\varepsilon}_1 & \partial\bar{\sigma}_1/\partial\bar{\varepsilon}_2 \\ \partial\bar{\sigma}_2/\partial\bar{\varepsilon}_1 & \partial\bar{\sigma}_2/\partial\bar{\varepsilon}_2 \end{bmatrix} + \begin{bmatrix} (\partial\bar{\sigma}_1/\partial\bar{\varepsilon}_3)(\partial\bar{\varepsilon}_3^*/\partial\bar{\varepsilon}_1) & (\partial\bar{\sigma}_1/\partial\bar{\varepsilon}_3)(\partial\bar{\varepsilon}_3^*/\partial\bar{\varepsilon}_2) \\ (\partial\bar{\sigma}_2/\partial\bar{\varepsilon}_3)(\partial\bar{\varepsilon}_3^*/\partial\bar{\varepsilon}_1) & (\partial\bar{\sigma}_2/\partial\bar{\varepsilon}_3)(\partial\bar{\varepsilon}_3^*/\partial\bar{\varepsilon}_2) \end{bmatrix} \right) \boldsymbol{T}^T \\ + \frac{\bar{\sigma}_1(\bar{\varepsilon}_1, \bar{\varepsilon}_2, \bar{\varepsilon}_3^*) - \bar{\sigma}_2(\bar{\varepsilon}_1, \bar{\varepsilon}_2, \bar{\varepsilon}_3^*)}{4(\bar{\varepsilon}_1 - \bar{\varepsilon}_2)} \begin{bmatrix} 1-\cos(4\theta) & \cos(4\theta)-1 & -\sin(4\theta) \\ & 1-\cos(4\theta) & \sin(4\theta) \\ \text{sym.} & & \cos(4\theta)+1 \end{bmatrix}, \end{aligned} \tag{17}$$

where

$$\frac{\partial\bar{\varepsilon}_3^*}{\bar{\varepsilon}_\alpha} = -\frac{\sum_{q=1}^{N_O} (1+\bar{\varepsilon}_\alpha)^{-1}(1+\bar{\varepsilon}_3)^{-1}\eta_q\alpha_q\beta_q J^{-\alpha_q\beta_q}}{\sum_{p=1}^{N_O} (1+\bar{\varepsilon}_3)^{\alpha_q-2}\eta_q(\alpha_q-1) + (1+\bar{\varepsilon}_3)^{-2}\eta_q(1+\alpha_q\beta_q)J^{-\alpha_q\beta_q}}, \quad \alpha = 1, 2, \tag{18}$$

and the expressions for the other quantities in (17) are the same as in the plane strain case.

Similarly to the plane strain case, when $\bar{\varepsilon}_1 = \bar{\varepsilon}_2$, the tangent modulus matrix $\boldsymbol{D}$ takes the following form

$$\begin{aligned} \boldsymbol{D} = & \begin{bmatrix} \partial\bar{\sigma}_1/\partial\bar{\varepsilon}_1 & \partial\bar{\sigma}_1/\partial\bar{\varepsilon}_2 & 0 \\ \partial\bar{\sigma}_2/\partial\bar{\varepsilon}_1 & \partial\bar{\sigma}_2/\partial\bar{\varepsilon}_2 & 0 \\ 0 & 0 & \frac{1}{2}(\partial\bar{\sigma}_1/\partial\bar{\varepsilon}_1 - \partial\bar{\sigma}_1/\partial\bar{\varepsilon}_2) \end{bmatrix} \\ & + \begin{bmatrix} (\partial\bar{\sigma}_1/\partial\bar{\varepsilon}_3)(\partial\bar{\varepsilon}_3^*/\partial\bar{\varepsilon}_1) & (\partial\bar{\sigma}_1/\partial\bar{\varepsilon}_3)(\partial\bar{\varepsilon}_3^*/\partial\bar{\varepsilon}_2) & 0 \\ (\partial\bar{\sigma}_2/\partial\bar{\varepsilon}_3)(\partial\bar{\varepsilon}_3^*/\partial\bar{\varepsilon}_1) & (\partial\bar{\sigma}_2/\partial\bar{\varepsilon}_3)(\partial\bar{\varepsilon}_3^*/\partial\bar{\varepsilon}_2) & 0 \\ 0 & 0 & \frac{1}{2}\partial\bar{\sigma}_1/\partial\bar{\varepsilon}_3(\partial\bar{\varepsilon}_3^*/\partial\bar{\varepsilon}_1 \\ & & -\partial\bar{\varepsilon}_3^*/\partial\bar{\varepsilon}_2) \end{bmatrix}. \end{aligned} \tag{19}$$

Moreover, in the limit, as the strain state $\boldsymbol{\varepsilon}$ goes to $\boldsymbol{0}$, $\boldsymbol{D}$ reduces to the standard material modulus for linear elasticity under plane stress condition [20].

3. Nonlinear finite element formulation

The nonlinear finite element formulation presented here follows references [11,18,26,49]. Consider a two-dimensional discretization Ω_h with boundary $\partial\Omega_h$ to be a finite element discretization (be it triangular, quadrilateral or polygonal) of the domain into a total of M non-overlapping finite elements with N nodes. We denote Γ_h^t and Γ_h^x to be the portions of the boundary where traction $\boldsymbol{t}$ (assumed to be independent of the displacement) and displacement are prescribed, respectively, such that $\Gamma_h^t \cap \Gamma_h^x = \varnothing$ and $\Gamma_h^t \cup \Gamma_h^x = \partial\Omega_h$. We also denote $E \in \Omega_h$ as a generic element of the mesh. Body forces are neglected throughout the paper.

The principle of minimum potential energy states that the equilibrating displacement $\boldsymbol{u}_h = \{u_{h,1}, u_{h,2}\}^T$ is the one that minimizes the potential energy Π_h among all the kinematically admissible displacements $\boldsymbol{v}_h$:

$$\Pi_h(\boldsymbol{u}_h) = \min_{\boldsymbol{v}_h \in \mathcal{K}_h} \left\{ \sum_{E \in \Omega_h} \int_E \Psi(\boldsymbol{\varepsilon}(\boldsymbol{v}_h)) \mathrm{d}\boldsymbol{x} - \int_{\Gamma_h^t} \boldsymbol{t} \cdot \boldsymbol{v}_h \mathrm{d}s \right\}, \tag{20}$$

where $\mathcal{K}_h$ stands for the finite dimensional displacement space. In the above expression, the first term on the right hand side is the internal energy of the discrete system and the second term is the external work done by the tractions.

The weak form of the Euler–Lagrange equations of the above minimization problem is given as

$$\delta\Pi_h(\boldsymbol{u}_h) = \sum_E \int_E \frac{\partial\Psi}{\partial\boldsymbol{\varepsilon}}(\boldsymbol{\varepsilon}(\boldsymbol{u}_h)) : \boldsymbol{\varepsilon}(\boldsymbol{v}_h) \mathrm{d}\boldsymbol{x} - \int_{\Gamma_h^t} \boldsymbol{t} \cdot \boldsymbol{v}_h \mathrm{d}s = 0 \quad \forall\, \boldsymbol{v}_h \in \mathcal{K}_h^0, \tag{21}$$

where $\mathcal{K}_h^0$ stands for the space of kinematically admissible displacements that vanish on Γ_h^x.

The subsequent discussion uses matrix-vector notation in order to provide a better connection with the computational implementation aspect of the nonlinear finite element formulation. Denoting $\boldsymbol{U} \in \mathbb{R}^{2N \times 1}$ as the vector collecting all of the nodal displacements of $\boldsymbol{u}_h$, we can rewrite expression (21) into a system of nonlinear equations following the standard finite element procedure:

$$\boldsymbol{R}(\boldsymbol{U}) = \frac{\partial\Pi_h}{\partial\boldsymbol{U}}(\boldsymbol{U}) = \boldsymbol{F}_{int}(\boldsymbol{U}) - \boldsymbol{F}_{ext} = \boldsymbol{0}, \tag{22}$$

where $\boldsymbol{F}_{int}(\boldsymbol{U})$, $\boldsymbol{F}_{ext}$ and $\boldsymbol{R}(\boldsymbol{U}) \in \mathbb{R}^{2N \times 1}$ are the internal force vector, the external force vector and the residual vector, respectively. Accordingly, the tangent stiffness matrix $\boldsymbol{K} \in \mathbb{R}^{2N \times 2N}$ of the nonlinear system of Eq. (22) is given by

$$\boldsymbol{K}(\boldsymbol{U}) = \frac{\partial\boldsymbol{R}}{\partial\boldsymbol{U}}(\boldsymbol{U}). \tag{23}$$

Note that, with only material nonlinearity considered, the global tangent stiffness matrix is guaranteed to be strictly positive definite provided that the tangent modulus matrix is strictly positive definite (no softening in the stress-strain relationship) and proper boundary conditions are applied. Consequently, the potential energy of the finite element discretization will be strictly convex and the equilibrating displacement field will be unique. On the contrary, when geometric nonlinearity is involved, the global tangent stiffness matrix $\boldsymbol{K}$ may lose positive definiteness even though the tangent modulus matrix $\boldsymbol{D}$ is positive definite, i.e., in the presence of geometric instability, and multiple solutions can occur [11,49]. These difficulties render the nonlinear finite element analysis involving geometrical nonlinearity considerably challenging in topology optimization problems in which the topologies are constantly updated.

In order to solve the system of nonlinear Eq. (22) in a robust manner, Newton's method, equipped with an inexact line search, is adopted [6,52]. Denoting the global nodal displacement vector at the kth iteration as $\boldsymbol{U}^{(k)}$, we update the nodal displacement vector in the subsequent iteration as

$$\boldsymbol{U}^{(k+1)} = \boldsymbol{U}^{(k)} + \xi^{(k)} \Delta\boldsymbol{U}^{(k)}, \tag{24}$$

where $\Delta\boldsymbol{U}^{(k)}$ is the update direction given by

$$\Delta\boldsymbol{U}^{(k)} = \boldsymbol{K}(\mathbf{U}^{(k)})^{-1}\boldsymbol{R}(\boldsymbol{U}^{(k)}), \tag{25}$$

and $\xi^{(k)}$ ($\xi^{(k)} \leq 1$) is the step size determined by an Armijo-type inexact line search rule [6]. The parameter $\xi^{(k)}$ is chosen such that a decrease of the potential energy is guaranteed in the updated displacement, namely,

$$\begin{aligned}\Pi_h(\boldsymbol{U}^{(k)}+\xi^{(k)}\Delta\boldsymbol{U}^{(k)}) &\le \Pi_h(\boldsymbol{U}^{(k)})+\tau\xi^{(k)}\left[\frac{\partial\Pi_h}{\partial\boldsymbol{U}}(\boldsymbol{U}^{(k)})\right]^T\Delta\boldsymbol{U}^{(k)}\\ &= \Pi_h(\boldsymbol{U}^{(k)})+\tau\xi^{(k)}\boldsymbol{R}(\boldsymbol{U}^{(k)})^T\Delta\boldsymbol{U}^{(k)}\end{aligned} \tag{26}$$

where τ is a user-defined guard constant (we chose $\tau = 10^{-4}$ in our implementation). Starting with $\xi^{(k)} = 1$, we employ a back-tracking algorithm to find the largest $\xi^{(k)}$ that satisfies condition (26) in our computational implementation. If the current step size $\xi^{(k)}$ violates condition (26), we reduce it according to: $\xi^{(k)} = \kappa\xi^{(k)}$, where the expression for the reduction factor κ is given by

$$\kappa = -\frac{\xi^{(k)}\boldsymbol{R}(\boldsymbol{U}^{(k)})^T\Delta\boldsymbol{U}^{(k)}}{2[\Pi_h(\boldsymbol{U}^{(k)}+\xi^{(k)}\Delta\boldsymbol{U}^{(k)})-\Pi_h(\boldsymbol{U}^{(k)})-\xi^{(k)}\boldsymbol{R}(\boldsymbol{U}^{(k)})^T\Delta\boldsymbol{U}^{(k)}]}. \tag{27}$$

If the calculated value of κ from the above equation is smaller than 0.1, we simply choose $\kappa = 0.5$. With the help of the aforementioned inexact line search rule, the Newton's method is ensured to converge to a stationary point of the potential energy [10], which is the unique solution provided that the potential energy is convex with respect to the displacement [37,52].

4. Topology optimization formulation

In this section, the topology optimization formulation considering hyperelastic material behavior under small deformation is presented. The matrix-vector convention introduced in the later part of Section 4 is adopted for the nonlinear finite element formulations. For the given discretization Ω_h, composed of a total of N nodes and M finite elements, the objective of the topology optimization problem is to maximize the potential energy of the structure at its equilibrium state, which essentially corresponds to maximizing the stiffness of the structure [25,29,30,37,52]. In particular, if we denote $\boldsymbol{\rho} \in \mathbb{R}^{M\times 1}$ as the vector of design variables, which take constant values between ϵ and 1 over each finite element where ϵ is a small positive number, we can express the nested optimization formulation as

$$\begin{aligned}&\min_{\boldsymbol{\rho}} \quad f(\boldsymbol{\rho}) = \min_{\boldsymbol{\rho}}[-\Pi_h(\boldsymbol{\rho}, \boldsymbol{U}(\boldsymbol{\rho}))]\\ &\text{s.t.} \quad g(\boldsymbol{\rho}) = \frac{\boldsymbol{A}^T\bar{\boldsymbol{\rho}}}{|\Omega_h|} - V_{\max} \le 0\\ &\qquad \epsilon \le \rho_e \le 1, \quad e = 1,\ldots,M\\ &\text{with} \quad \boldsymbol{R}(\boldsymbol{\rho}, \boldsymbol{U}(\boldsymbol{\rho})) = \boldsymbol{F}_{int}(\boldsymbol{\rho}, \boldsymbol{U}(\boldsymbol{\rho})) - \boldsymbol{F}_{ext} = \boldsymbol{0},\end{aligned} \tag{28}$$

where $\boldsymbol{A} \in \mathbb{R}^{M\times 1}$ is a vector containing the area of each element and $\bar{\boldsymbol{\rho}} \in \mathbb{R}^{M\times 1}$ is a vector of filtered design variables. The parameter $\epsilon << 1$ is a positive number assigned in order to prevent the tangent stiffness matrix $\boldsymbol{K}$ from becoming singular [3,4,13,21].

To regularize the optimization problem, we adopt the commonly used density filtering approach [12]. The filtered design variable $\bar{\rho}_e$, of element E_e, is computed via a convolution operator of the design variable ρ_e with its surrounding design variables as

$$\bar{\rho}_e = \frac{\sum_{j\in S(e)}\rho_k|E_j|(1-|\boldsymbol{x}_e^c-\boldsymbol{x}_j^c|/R)}{\sum_{k\in S(e)}|E_k|(1-|\boldsymbol{x}_e^c-\boldsymbol{x}_k^c|/R)}, \tag{29}$$

where $S(e)$ is the set of indices of element E_k whose centroid, $\boldsymbol{x}_k^c$, falls within in a prescribed radius R of the centroid, $\boldsymbol{x}_e^c$, of element E_e. For meshes consists of uniform elements, the terms $|E_k|$ and $|E_j|$ (the areas or volumes of elements E_k and E_j, respectively) are typically omitted in the above expression, which is the case in our paper. We also note that one can alternatively expressed filter operation in the matrix notation as [42]

$$\bar{\boldsymbol{\rho}} = \boldsymbol{P}\boldsymbol{\rho}, \tag{30}$$

where the (e, j) component of $\boldsymbol{P} \in \mathbb{R}^{M\times M}$ is given as

$$P_{ej} = \frac{\max(0, (1-|\boldsymbol{x}_e^c-\boldsymbol{x}_j^c|/R))}{\sum_{k\in S(e)}(1-|\boldsymbol{x}_e^c-\boldsymbol{x}_k^c|/R)}. \tag{31}$$

The potential energy Π_h at the equilibrium state is given by

$$\Pi_h(\boldsymbol{\rho}, \boldsymbol{U}(\boldsymbol{\rho})) = \sum_{E_e\in\Omega_h}\int_{E_e}\Psi(\rho_e, \boldsymbol{\varepsilon}(\boldsymbol{U}(\boldsymbol{\rho})))\mathrm{d}\boldsymbol{x} - \boldsymbol{F}_{ext}^T\boldsymbol{U}(\boldsymbol{\rho}), \tag{32}$$

and the stored-energy function in the eth element $\Psi(\rho_e, \boldsymbol{\varepsilon}(\boldsymbol{U}(\rho)))$ is interpolated using the SIMP [8,9,38] relationship as

$$\Psi(\rho_e, \underline{\boldsymbol{\varepsilon}}(\boldsymbol{U}(\boldsymbol{\rho}))) = (\bar{\rho}_e)^p\Psi_0(\boldsymbol{\varepsilon}(\boldsymbol{U}(\boldsymbol{\rho}))). \tag{33}$$

where Ψ_0 denotes the stored-energy function for solid material and p is the penalization factor. We note that, for linear problem, this potential energy reduces to the negative compliance of the structure, that is, $\Pi_h(\boldsymbol{\rho}, \boldsymbol{U}(\boldsymbol{\rho})) = -1/2\boldsymbol{F}_{ext}^T\boldsymbol{U}(\boldsymbol{\rho})$ [29]. Therefore, the optimization formulation (28) reduces to the classic compliance-minimization optimization when the material behaves linearly.

The sensitivity for the objective function is given by

$$\frac{\partial f}{\partial\rho_e}(\boldsymbol{\rho}) = -\frac{\partial\Pi_h}{\partial\rho_e}(\boldsymbol{\rho}, \boldsymbol{U}(\boldsymbol{\rho})) - \frac{\partial\Pi_h}{\partial\boldsymbol{U}}(\boldsymbol{\rho}, \boldsymbol{U}(\boldsymbol{\rho}))\frac{\partial\boldsymbol{U}}{\partial\rho_e}(\boldsymbol{\rho}). \tag{34}$$

Because equilibrium is satisfied for the structure at each optimization step, the second term of the sensitivity vanishes according to (22). We can simplify the above expression for the sensitivity of the objective function as

$$\begin{aligned}\frac{\partial f}{\partial\rho_e}(\boldsymbol{\rho}) &= -\sum_{k=1}^{M}\frac{\partial\Pi_h}{\partial\bar{\rho}_k}(\boldsymbol{\rho}, \boldsymbol{U}(\boldsymbol{\rho}))\frac{\partial\bar{\rho}_k}{\partial\rho_e}\\ &= -p\sum_{k=1}^{M}P_{ke}(\bar{\rho}_k)^{p-1}\int_{E_k}\Psi_0(\underline{\boldsymbol{\varepsilon}}(\boldsymbol{U}(\boldsymbol{\rho})))\mathrm{d}\boldsymbol{x},\end{aligned} \tag{35}$$

where we recall that P_{ke} is the (k, e) component of the projection matrix $\boldsymbol{P}$ defined in (31). Because the volume constraint is linear, its sensitivity is simply given by

$$\frac{\partial g}{\partial\boldsymbol{\rho}} = \frac{\boldsymbol{P}^T\boldsymbol{A}}{|\Omega_h|}. \tag{36}$$

We remark that no adjoint equation needs to be solved in calculating the sensitivity of the objective function. Additionally, the sensitivity is guaranteed to be non-positive, which also ensures that we can confidently use the efficient Optimality Criteria (OC) method to update the design variables. For the $k$the optimization step with design variable $\rho^{(k)}$, the OC method update the design variable as follows

$$\rho_e^{(k+1)} = \begin{cases}\max(\varepsilon, \rho_e^{(k)} - move) & \text{if } \rho_e^{(k)}(B_e)^\eta \le \max(\varepsilon, \rho_e^{(k)} - move)\\ \min(1, \rho_e^{(k)} + move) & \text{if } \rho_e^{(k)}(B_e)^\eta \ge \min(1, \rho_e^{(k)} + move)\\ (B_e)^\eta & \text{otherwise,}\end{cases} \tag{37}$$

where *move* is a the move limit and η is the damping ratio. B_e is defined as

$$B_e = -\frac{\partial f/\partial\rho_e}{\lambda\partial g/\partial\rho_e}\Big|_{\boldsymbol{\rho}=\boldsymbol{\rho}^{(k)}}, \tag{38}$$

where λ is the optimal Lagrangian multiplier determined through a bisection approach so that the volume constraint is satisfied.

5. Numerical examples

This section presents four numerical examples that utilize the Ogden-based constitutive model proposed in Section 2 to demonstrate the influences of material parameters, load levels and loading conditions (plane strain vs. plane stress) on the layout of the optimal topology. We highlight that, in all the numerical examples, the nonlinear finite element simulations are stable and the convergence histories are smooth for fixed penalization parameter p and filter radius R.

In terms of the nonlinear finite element modeling, we consider a quadrilateral mesh in the first example and polygonal meshes in the

remaining examples. The polygonal meshes are constructed using the software "PolyMesher" [41] and are solved using the polygonal finite element method with Wachspress shape functions [47]. To integrate the internal force vector and stiffness matrix of the polygonal finite elements, we use a 1st order triangulation rule together with the gradient correction scheme of reference [19]. The Newton's method is regarded as converged once the normalized residual vector $||\boldsymbol{R}||/||\boldsymbol{F}_{ext}||$ is less than 10^{-5} times of its initial value.

In terms of the optimization process, the OC update scheme (37) is used for all the numerical examples. Its damping factor and the move limit are taken to be $\eta = 0.5$ and $move = 0.2$, respectively. For all the examples, uniform initial guesses are used, which take the values of $\rho^0 = V_{\max}$ for all the elements in the mesh. With the convex material model, the optimization problem is proven to be convex when penalization parameter $p = 1$ [37,52]. Thus, similar to the classic minimum compliance problem considering linear materials, we adopt a continuation of the penalization parameter p in order to achieve better solutions [40]. The penalization parameter p is updated every two iterations by $p = p + \Delta p$ with $\Delta p = .1$ until a maximum value of $p = 3$ is reached. In addition, we also employ continuation scheme of the radius R of the density filter in order to approach black and white designs. We first conduct optimization with an initial filter radius $R = R_0$ until either convergence ($TOL = 0.05$) or a prescribed maximum iteration number ($Iter_{\max} = 200$) is achieved. The filter radius is then updated every 10 iterations by $R = R - \Delta R$ with $\Delta_R = R_0/4$ until a minimum value $R = R_0/4$ is reached.

Furthermore, all the numerical examples consider a one term stored-energy function, i.e, $N_O = 1$ in (6). For this particular case, we have three independent material parameters, α_1, β_1 and η_1. Among them, α_1 is a user-prescribed parameter that dictates the level of nonlinearity in the stress-strain curve. We remark that, although the Ogden models are typically used for modeling elastomers and biological tissues with positive α_1, this work also includes Ogden models with negative α_1 because, from an optimization/design perspective, it allows us to consider material behaviors with larger compressive stiffness than the tensile one, such as concrete. Once α_1 is prescribed, the other two parameters, β_1 and η_1, are determined by the Young's modulus E_0 and Poisson's ratio ν of the solid via

$$\eta_1 = \frac{E_0}{\alpha(1+\nu)} \quad \text{and} \quad \beta_1 = \frac{\nu}{1-2\nu}. \tag{39}$$

Under plane stress condition, an explicit expression can be obtained for the out-of-plane principal strain $\bar{\varepsilon}_3$ by solving the nonlinear algebraic Eq. (16) as

$$\bar{\varepsilon}_3 = [(1+\bar{\varepsilon}_1)(1+\bar{\varepsilon}_2)]^{-\frac{\nu}{1-\nu}} - 1. \tag{40}$$

In Fig. 1 (a) and (b), we plot the stress-strain responses $\bar{\sigma}_1$ vs. $\bar{\varepsilon}_1$ under biaxial stretch (i.e. $\bar{\varepsilon}_2 = 0$ and $\bar{\sigma}_2 \neq 0$) for the plane strain and plane stress conditions, respectively. Each figure considers two distinct α_1, namely $\alpha_1 = 1500$ and $\alpha_1 = -1500$. For all the cases, Young's Modulus and Poisson's ratio are taken to be $70MPa$ and 0.3, respectively. It can be observed from the figures that varying the material parameter α_1 generates distinctive stress-strain response. For a solid with $\alpha_1 = 1500$, the response behavior in tension dominates under both plane strain and plane stress conditions. For a solid with $\alpha_1 = -1500$, we observe the opposite behavior. Moreover, we also notice that the behavior is different under plane strain and plane stress conditions. For instance, the solid with $\alpha_1 = 1500$ exhibits more apparent hardening behavior in compression under the plane strain condition than under the plane stress condition.

The proposed topology optimization is computationally efficient in the following two aspects. First, the adopted objective function does not require solving an adjoint system. Second, the inexact line search strategy greatly improves the robustness of Newton's method in solving nonlinear state equations and thus, avoids the need for multiple load steps, even for high load levels. Since solving the nonlinear state equation is always the most time-consuming part in nonlinear topology optimization, this can improve the computational efficiency of the nonlinear topology optimization.

5.1. Example 1: A simply supported square domain with a central load

In the first numerical example, the design domain is a 1 m by 1 m square simply supported on the mid-points of its left and right sides. As depicted in Fig. 2, a load $F = 1000$ N acts at the center of the square domain. The design domain is discretized by 200 by 200 structured quadrilateral elements. For the topology optimization, we prescribe the

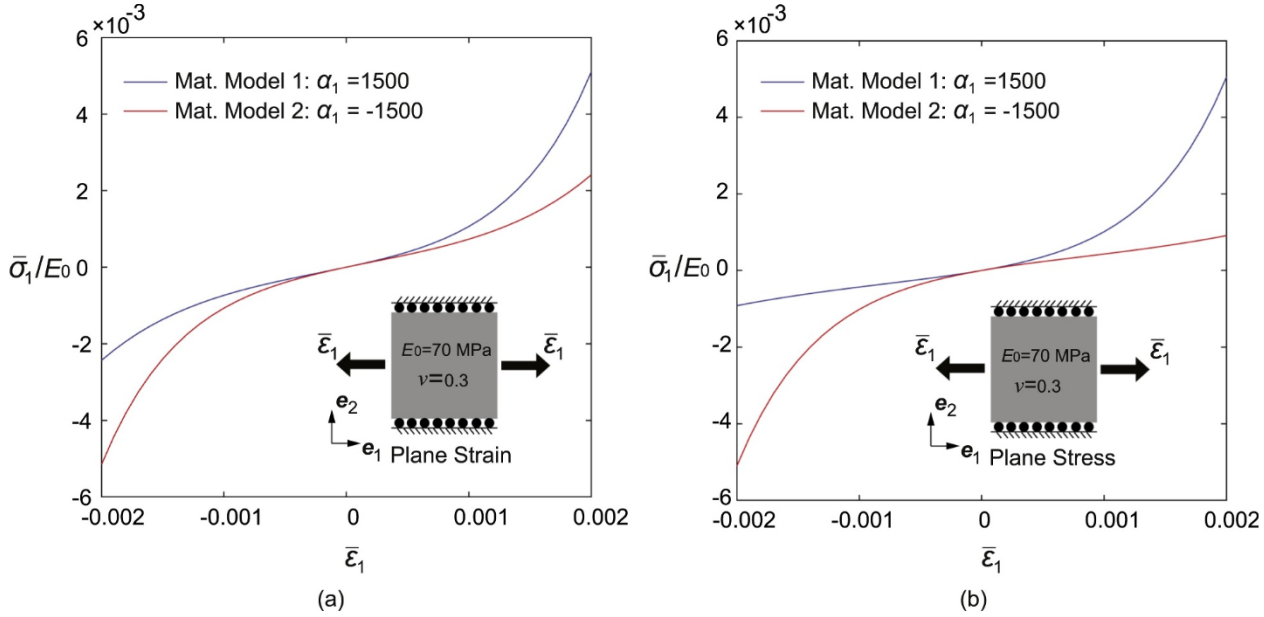

Fig. 1. Stress-strain curves $\bar{\sigma}_1$ v.s. $\bar{\varepsilon}_1$ under biaxial stretch with (a) plane strain condition (i.e. $\bar{\varepsilon}_2 = 0$ and $\bar{\sigma}_2 = E_0/\alpha_1/(1+\nu)\left[1-(1+\bar{\varepsilon}_1)^{-\alpha_1\nu/(1-2\nu)}\right]$) and (b) plane stress condition (i.e. $\bar{\varepsilon}_2 = 0$ and $\bar{\sigma}_2 = E_0/\alpha_1/(1+\nu)\left\{1-[(1+\bar{\varepsilon}_1)(1+\bar{\varepsilon}_3)]^{-\alpha_1\nu/(1-2\nu)}\right\}$).

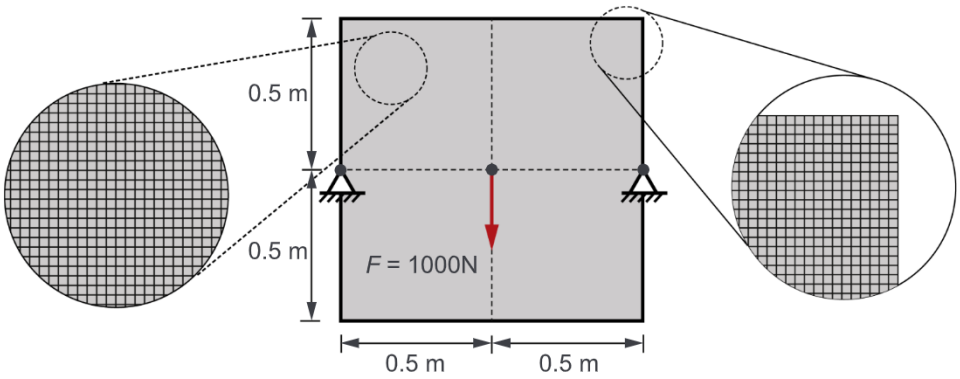

Fig. 2. Illustration of the design domain and its load and boundary conditions.

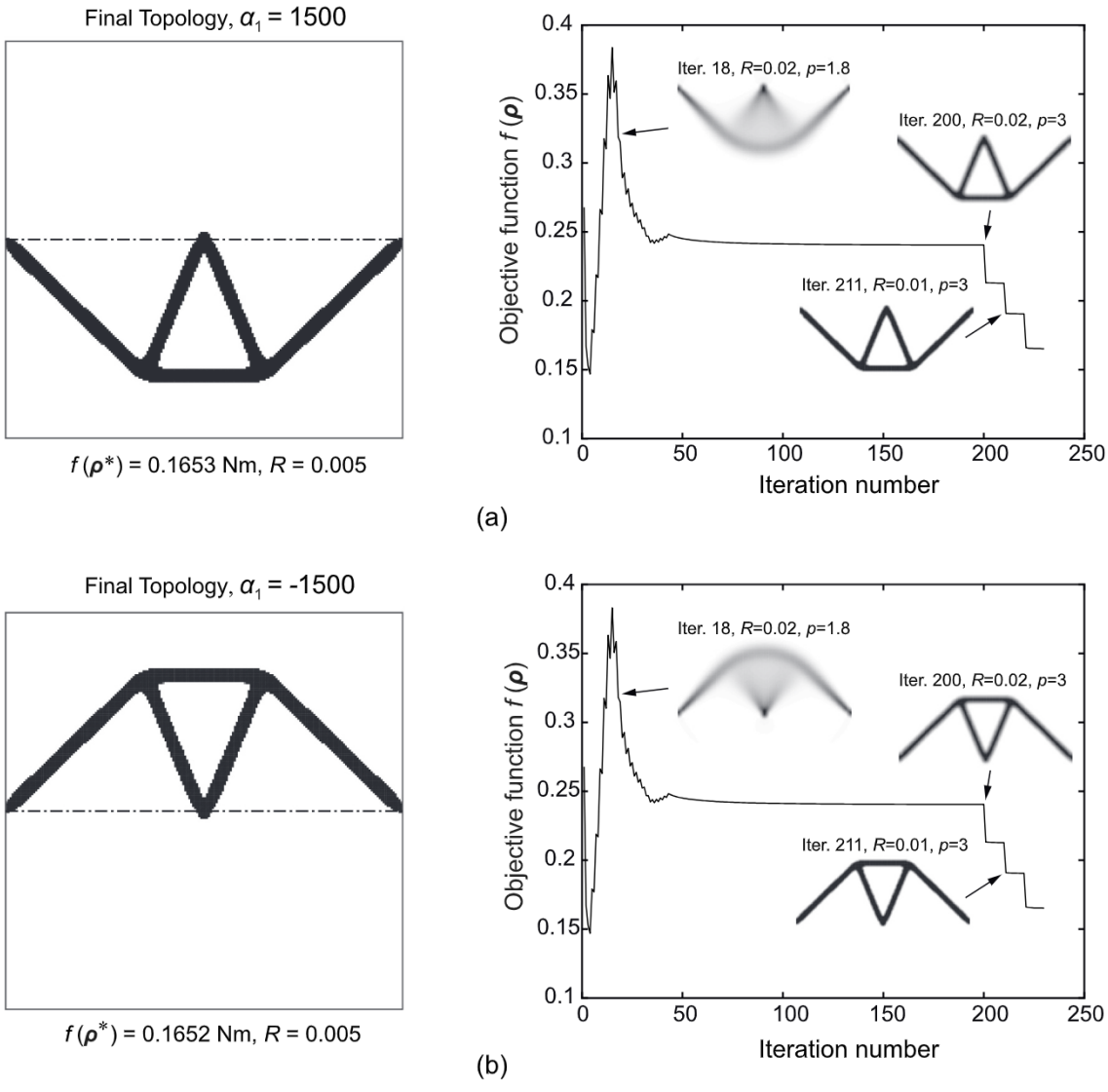

Fig. 3. Optimal topologies and convergence histories of the objective function for Example 1 considering (a) material with $\alpha_1 = 1500$ and (b) material with $\alpha_1 = -1500$. We note that all the jumps in the convergence histories of the objective function are due to either the increase of penalization parameter p or the decrease of the filter radius R.

volume fraction to be 15% (i.e. $V_{max} = 0.15$) and the initial filter radius to be $R_0 = 0.02$ m. In order to study the influence of the material parameter α_1 on the final topologies, we consider two materials with α_1 equal to 1500 and − 1500, respectively (see Fig. 1). The Young's Modulus E_0 and Poisson's ratio ν of both materials are $E_0 = 70$ MPa and $\nu = 0.3$. The plane strain condition is assumed (see Fig. 1 (a)). Figures 3 (a) and (b) show the final topologies and the convergence histories of the objective function for the two materials ($\alpha_1 = 1500$ and $\alpha_1 = -1500$). We observe that, although the objective values are almost identical, the optimal topologies obtained for the two materials are completely different: the one composed of the material with $\alpha_1 = 1500$ is in the lower half of the design domain while the one composed of the material with $\alpha_1 = -1500$ is in the upper half of the design domain. The difference in the optimal topologies is due to the difference in tensile and compressive responses of the two materials (see Fig. 1 (a)). For instance, the material with $\alpha_1 = 1500$ is stronger in tension than in compression; thus, it performs better with structures that are dominated by tension members (i.e., structures that mainly occupy the lower half design domain). Regarding the convergence history, we remark that the optimization problem possesses smooth convergence and all the jumps in the convergence plots are caused by either increasing the penalization parameter p or decreasing of the filter radius R.

5.2. Example 2: A simply supported rectangle domain with opposite loads

Unlike topology optimization considering linear material behavior, which yields identical optimal topology regardless of the load levels, topology optimization considering nonlinear material behavior allows us to study the influence of the load level on the layout of the optimal topologies. To demonstrate this point, we consider the design problem illustrated in Fig. 4 (a), where a 2 m by 1 m rectangular design domain is simply supported on the mid-points of its left and right boundaries. The design domain is subjected to two loads of equal magnitude F pointing in opposite directions and each acting on a point that is 0.7 m away from the supports. While fixing the material parameters as $E_0 = 70$ MPa, $\nu = 0.3$ and $\alpha_1 = 1500$, we consider three load levels: (i) $F = 50$ N (small), (ii) $F = 5000$ N (medium), and (iii) $F = 50000$ N (large). We prescribe the volume fraction to be 7% (i.e. $V_{max} = 0.07$) and the initial filter radius to be $R_0 = 0.03$ m. In the finite element analysis, plane strain conditions are considered and the design domain is discretized by a Centroidal Vornoi Tessellation (CVT) mesh as shown in Fig. 4 (a). The CVT mesh is made up of 40,000 polygonal finite elements whose statistics provided in Fig. 4 (b). In Fig. 5 (a)–(c), we show the optimal topologies obtained by the three load cases (i)–(iii), respectively, as well as the corresponding plots of convergence histories of objective functions. When considering linear materials, the optimal topology will always be identical to the one obtained with the small load level (level i)). However, when nonlinear material behavior is considered, completely distinctive optimal topologies are obtained for the three load levels. It is observed from Fig. 5 (a)–(c) that, as the load level increases, the members in the optimal topologies become thicker.

In order to demonstrate the effectiveness of the line search scheme in improving the convergence of the standard Newton's method, we provide Tables 1 and 2 that summarize the convergence histories of the nonlinear FE analysis in the 1st optimization step. Table 1 lists those without the line search scheme (i.e. ξ is always equal to 1), while Table 2 lists the history of the normalized residual vector $||\boldsymbol{R}||/||\boldsymbol{F}_{ext}||$ when the line search scheme is applied. It is apparent from the comparison between the two tables that introduction of the line search scheme in the Newton's method significantly improves the convergence performance. While the standard Newton's method (without line search) quickly diverges after the 1st nonlinear FE iteration for medium and large load levels (see Table 1), incorporation of the line search scheme ensures convergence of the nonlinear FE analysis in a reasonable number of iterations for all load levels (see Table 2). This indicates the effectiveness of the line search scheme in improving the robustness of the nonlinear FE analysis, which may otherwise need multiple loading steps, and eventually lead to the robustness of the optimization process. From a computational perspective, the inexact line search scheme constitutes a small fraction of the computational time in solving the nonlinear state equations because it only requires several evaluations of the potential energy function of the systems.

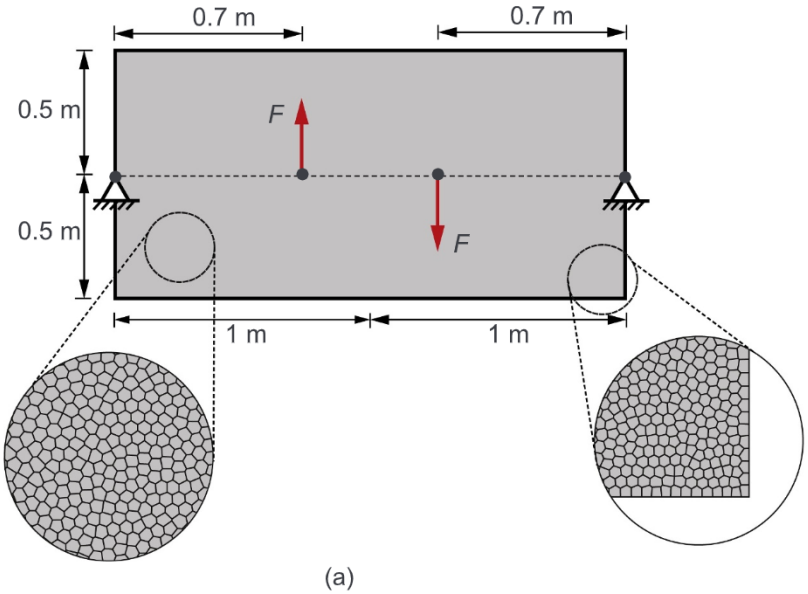

n	n-gon	# of n-gons
4	□	44
5	⬠	5,407
6	⬡	30,467
7	⬡	4,081
8	⬡	1
# of Elements		40,000

(b)

Fig. 4. (a) Illustration of the design domain with load and boundary conditions for Example 2. (b) Statistics of the composition of the CVT mesh.

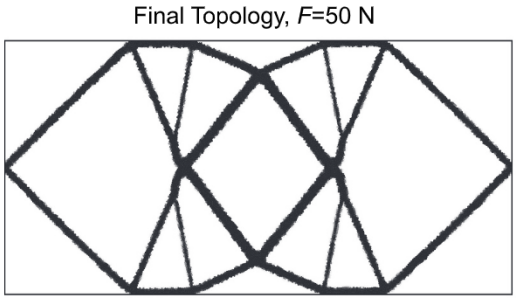

$f(\boldsymbol{\rho}^*)$= 3.2487E-04 Nm, R=0.0075

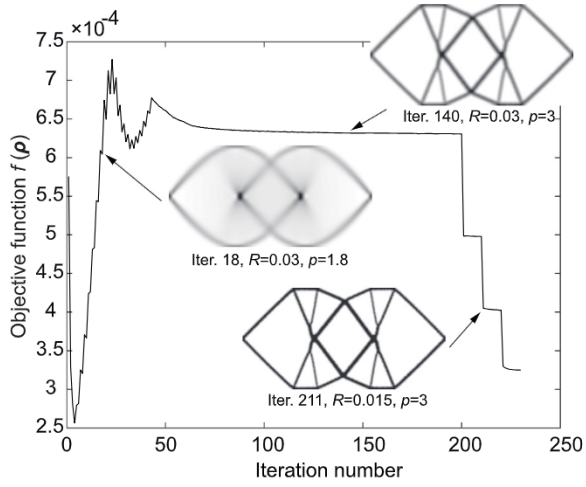

(a)

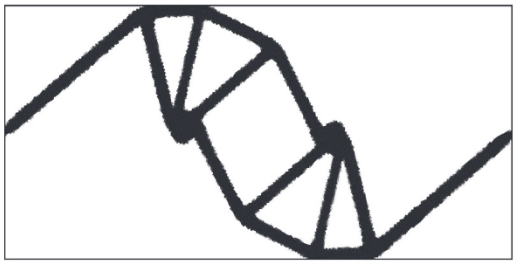

$f(\boldsymbol{\rho}^*)$= 3.0265 Nm, R=0.0075

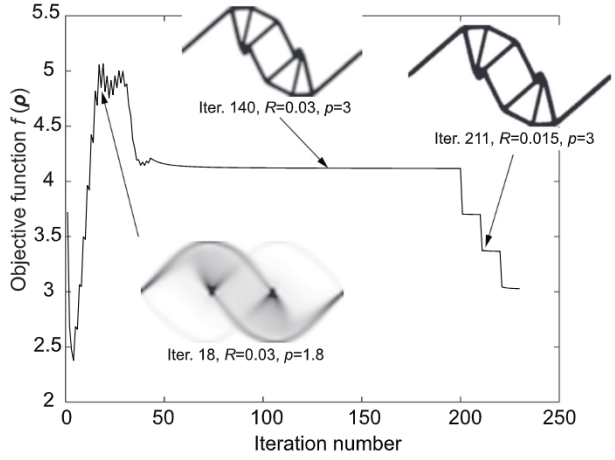

(b)

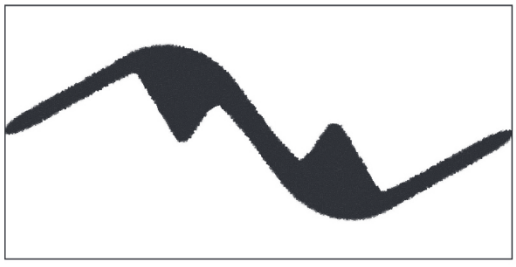

$f(\boldsymbol{\rho}^*)$= 163.1779 Nm, R=0.0075

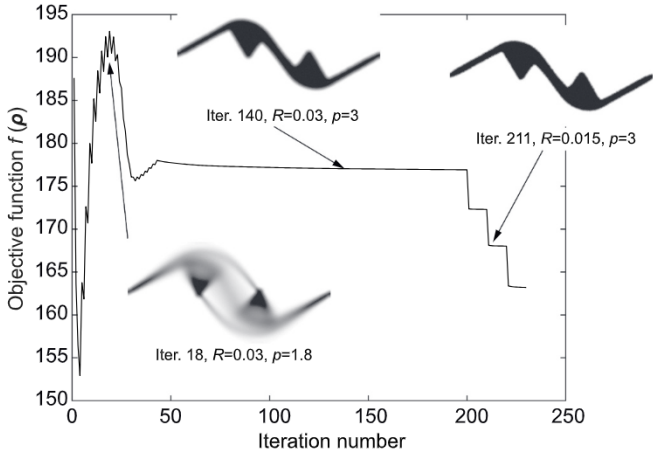

(c)

Fig. 5. Optimal topologies and convergence histories of the objective function for Example 2 considering (a) a small load level $F = 50$ N, (b) a medium load level $F = 5000$, and (c) a large load level $F = 50000$. Again, we stress that all the jumps in the convergence histories of the objective function are due to either the increase of penalization parameter p or the decrease of the filter radius R.

Table 1
Convergence history of the normalized residual vector in the FE analysis, during the 1st optimization step, without application of line search (step length $\xi = 1$).

F = 50 N			F = 5000 N			F = 50000 N		
Iter.	ξ	$\|\|\boldsymbol{R}\|\|/\|\|\boldsymbol{F}_{ext}\|\|$	Iter.	ξ	$\|\|\boldsymbol{R}\|\|/\|\|\boldsymbol{F}_{ext}\|\|$	Iter.	ξ	$\|\|\boldsymbol{R}\|\|/\|\|\boldsymbol{F}_{ext}\|\|$
1	1	1	1	1	1	1	1	1
2	1	5.19×10^{-2}	2	1	5.70×10^{23}	2	1	6.00×10^{22}
3	1	4.18×10^{-4}		$\|\|\boldsymbol{R}\|\|/\|\|\boldsymbol{F}_{ext}\|\| \to \infty$			$\|\|\boldsymbol{R}\|\|/\|\|\boldsymbol{F}_{ext}\|\| \to \infty$	
4	1	2.80×10^{-8}						

Table 2
Convergence history of the normalized residual vector in the FE analysis, during the 1st optimization step, with application of line search .

F = 50 N			F = 5000 N			F = 50000 N		
Iter.	ξ	$\|\|\boldsymbol{R}\|\|/\|\|\boldsymbol{F}_{ext}\|\|$	Iter.	ξ	$\|\|\boldsymbol{R}\|\|/\|\|\boldsymbol{F}_{ext}\|\|$	Iter.	ξ	$\|\|\boldsymbol{R}\|\|/\|\|\boldsymbol{F}_{ext}\|\|$
1	1	1	1	1	1	1	1	1
2	1	5.19×10^{-2}	2	0.125	6.37	2	0.0156	3.81
3	1	4.18×10^{-4}	3	0.4725	3.87	3	0.125	5.60
4	1	2.80×10^{-8}	4	1	1.28	4	0.1812	4.67
			5	1	3.36×10^{-1}	5	1	1.74
			6	1	4.94×10^{-2}	6	1	5.20×10^{-1}
			7	1	1.70×10^{-3}	7	1	1.29×10^{-1}
			8	1	2.50×10^{-6}	8	1	2.16×10^{-2}
						9	1	1.10×10^{-3}
						10	1	4.33×10^{-6}

5.3. Example 3: Top central load in a laterally constrained rectangular domain

In the third numerical example, we demonstrate the effect of loading states, i.e., plane strain v.s. plane stress conditions, on the layout of the optimal topologies. As illustrated by Fig. 6 (a), we consider a problem where a rectangular beam of dimensions 3 m by 1 m is fixed on both left and right ends and subjected to a downward load at the center of its top edge. In the optimization, the volume fraction is set to 15% (i.e. $V_{\max} = 0.15$) and the initial radius is chosen as $R_0 = 0.04$ m. In terms of the FE analysis, the design domain is discretized by a CVT mesh composed of 40,000 elements, as shown in Fig. 6 (a), whose statistics of composition is provided in Fig. 6 (b). While fixing the material properties to be $E_0 = 70$ MPa, $\nu = 0.3$ and $\alpha_1 = 1500$, we consider both plane strain and plane stress conditions and two load levels $F = 4000$ N and $F = 5000$ N. For the lower load level ($F = 4000$ N), Fig. 7 (a) and (b) show the optimal topologies, convergence histories and optimization histories for the plane strain and plane stress conditions respectively. Similarly, Fig. 8 (a) and (b) show the optimal topologies, convergence histories and optimization histories for the plane strain and plane stress conditions, respectively, in the case of the higher load level ($F = 5000$ N). By comparing Figs. 7 and 8, we conclude that, as we increase the load from $F = 4000$ N to $F = 5000$ N, the optimal topology stays unchanged when the plane strain condition is assumed. On the contrary, when assuming the plane stress condition, the optimal topology obtained at the lower load level ($F = 4000$ N) significantly differs from that obtained at the higher load level ($F = 5000$ N). Based on Fig. 1 (a) and (b), an explanation of the

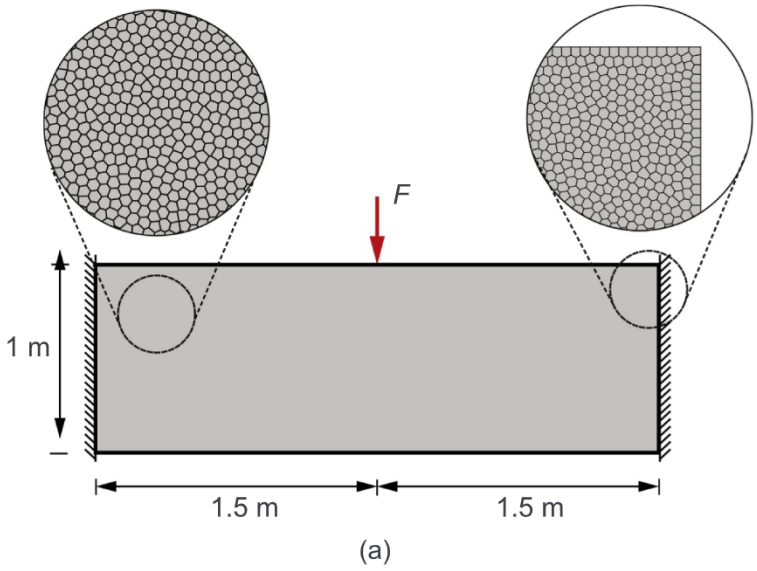

n	n-gon	# of n-gons
4		60
5		5,476
6		30,464
7		3,998
8		2
# of Elements		40,000

(b)

Fig. 6. (a) Illustration of the design domain with load and boundary conditions for Example 3. (b) Statistics of the composition of the CVT mesh.

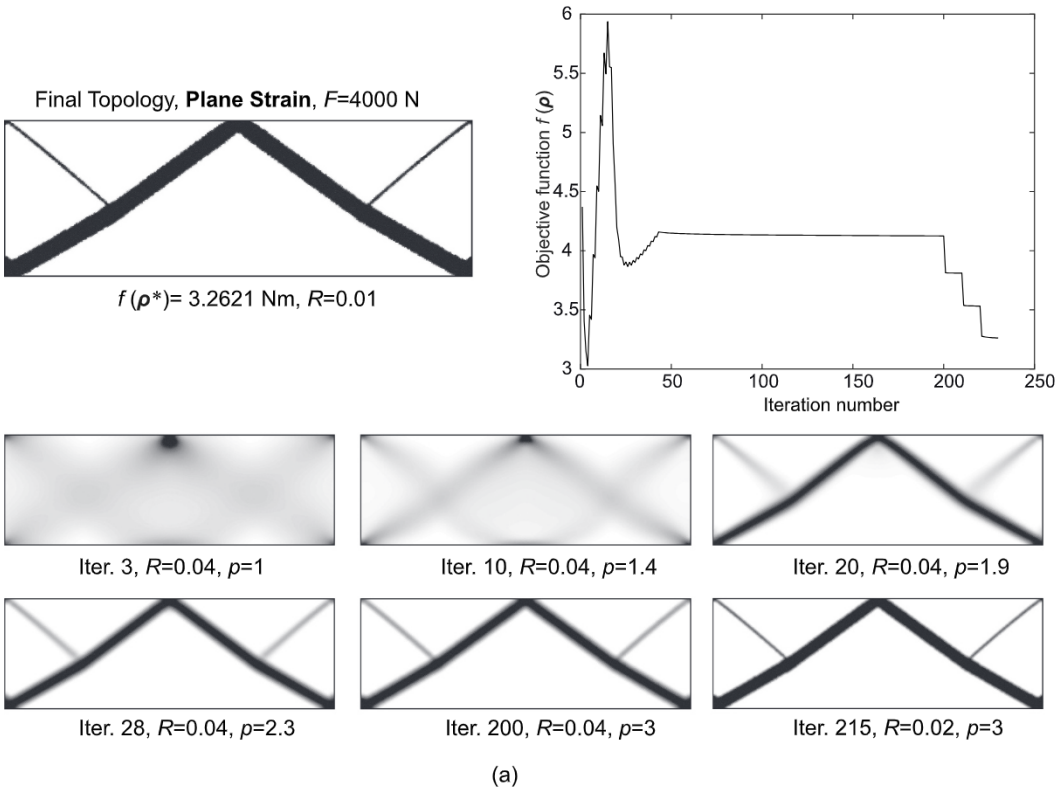

Fig. 7. Optimal topologies, convergence histories and optimization histories in the case of the lower load level $F = 4000$ N for (a) the plane strain and (b) the plane stress conditions. Note: both optimal solutions are quite similar (cf. Fig. 8).

above described difference in the optimal topologies under the plane strain and plane stress conditions is that, although the material behaves similarly in tension under the plane strain and stress conditions, its behavior in compression is different under these two conditions – the material is considerably softer under the plane stress condition than under the plane strain condition at higher levels of compressive strain (for $\alpha_1 = 1500$). When plane stress condition is assumed, this softer compressive behavior of the material promotes the final topology to

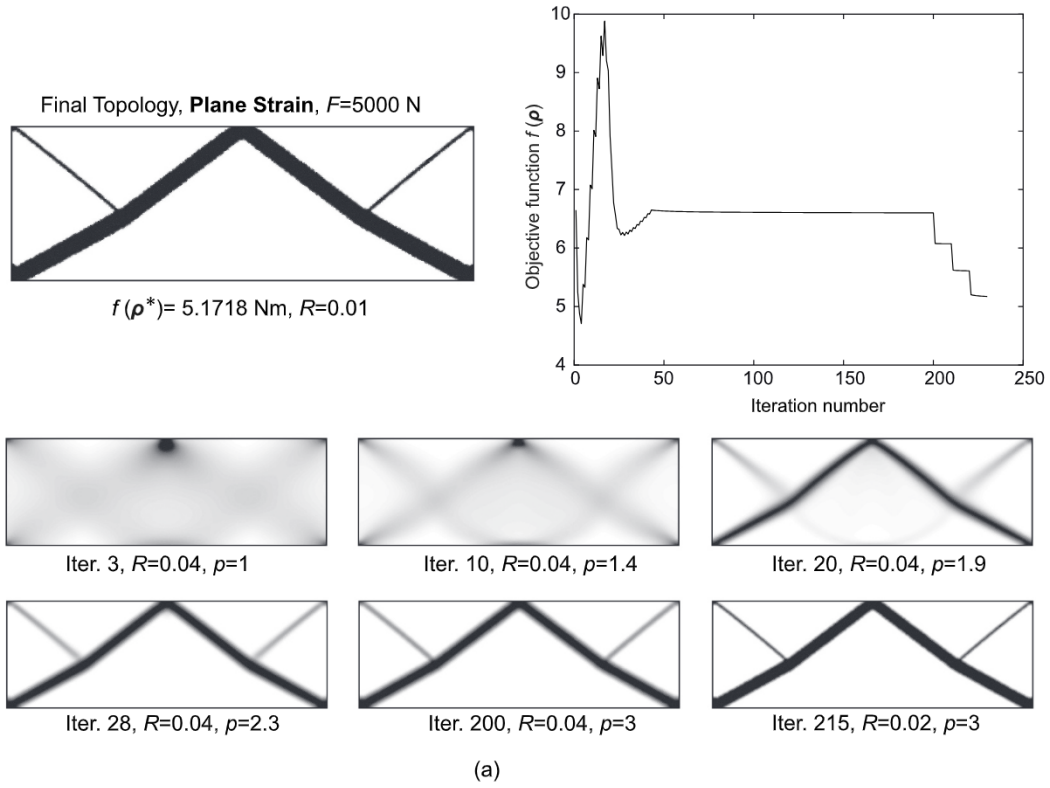

(a)

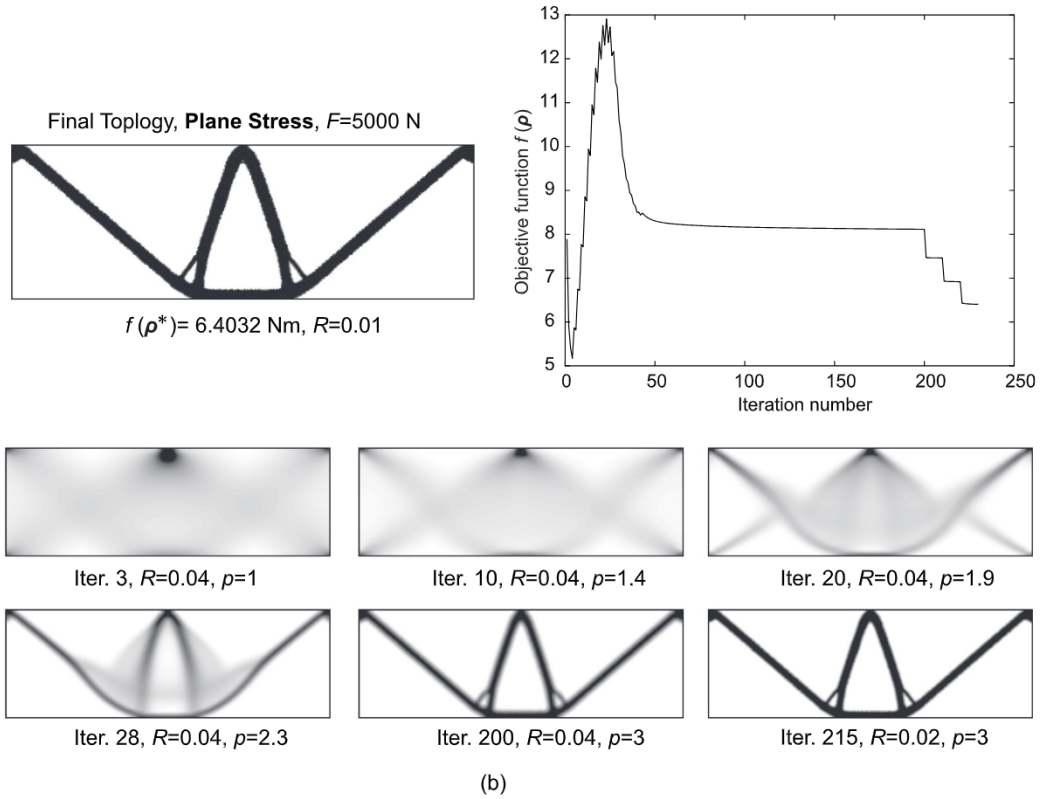

(b)

Fig. 8. Optimal topologies, convergence histories and optimization histories in the case of the higher load level $F = 5000$ N for (a) the plane strain and (b) the plane stress conditions. Note: optimal solutions are quite different (cf. Fig. 7).

change from a compression dominated structure to a tension dominated structure at the higher load level.

5.4. Example 4: A bridge design

Finally, we use the last example to demonstrate the influence of nonlinear material properties on practical designs. To this end, we consider a bridge design problem adapted from [5]. The dimensions and boundary conditions of this problem are shown in Fig. 9. In the design domain, a non-designable layer ($\rho = 1$) of thickness 2 m is placed at the height of 20 m, representing the bridge deck, and a uniformly distributed load q = 5 KN/m is applied on top of the non-designable layer. This design domain is then discretized by a mesh consisting of 43200 structured quadrilateral elements in the FE analysis. As

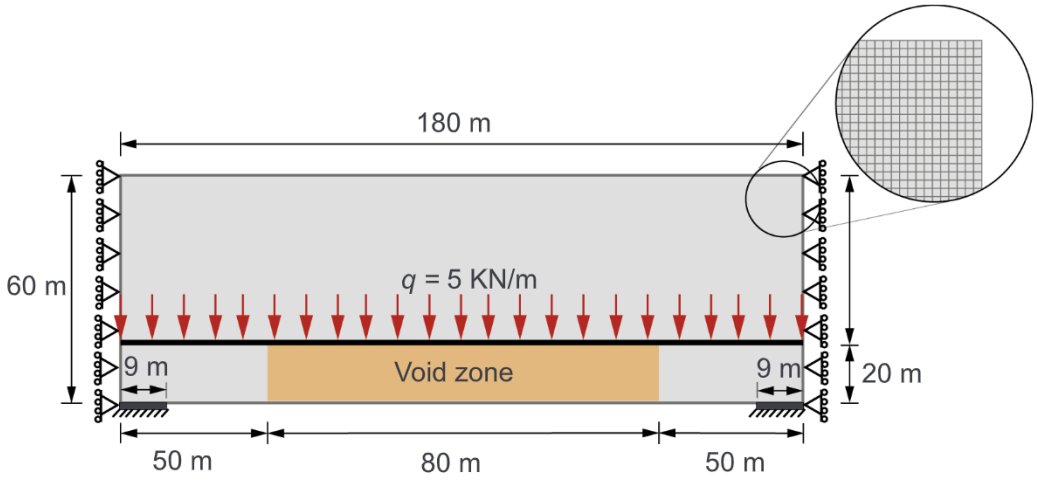

Fig. 9. (a) Illustration of the design domain with load and boundary conditions for Example 4.

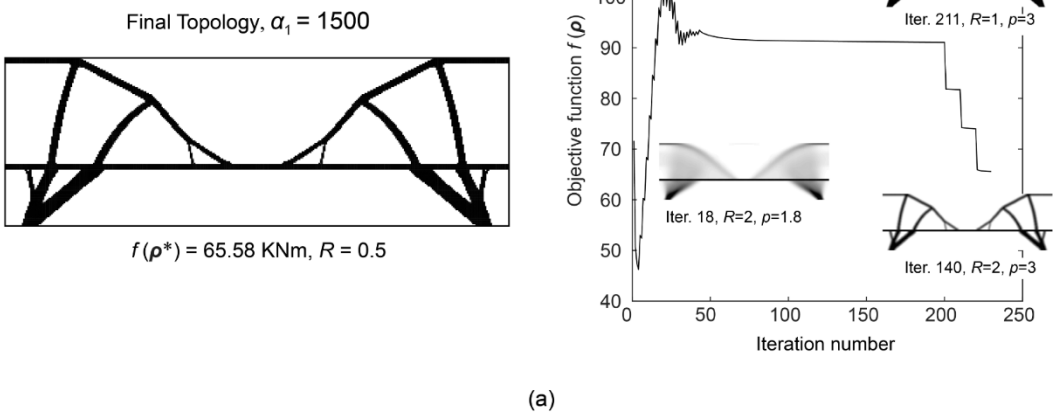

(a)

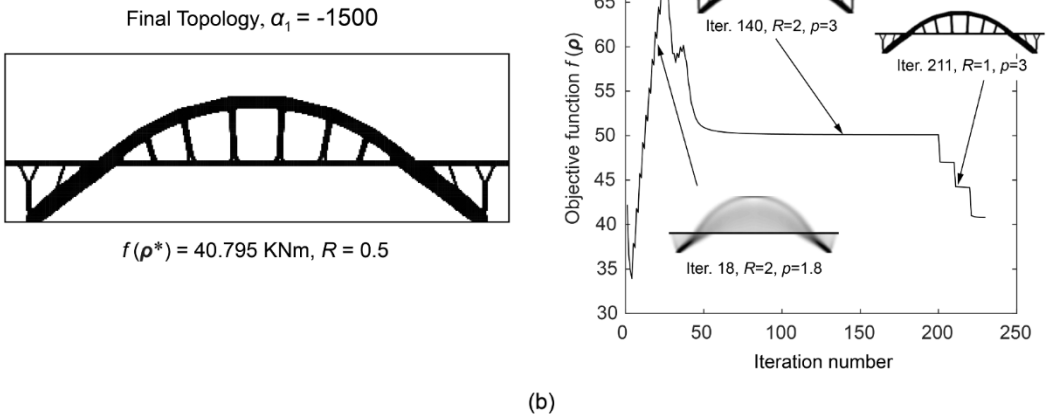

(b)

Fig. 10. Optimal topologies and convergence histories of the objective function for the bridge design example considering (a) material with $\alpha_1 = 1500$ and (b) material with $\alpha_1 = -1500$. We note that all the jumps in the convergence histories of the objective function are due to either the increase of penalization parameter p or the decrease of the filter radius R.

for the optimization parameters, the total volume fraction (including the non-designable layer) is assumed to be $V_{max} = 15\%$ and the initial filter radius is taken to be R = 2 m. Moreover, throughout the optimization process, once a supported node is completely surrounded by void elements (i.e. $\rho \leq 0.01$, we remove the support on this node in the FE analysis.) Assuming the plane stress condition, we consider two materials with the same Young Modulus ($E_0 = 70$ MP) and Poisson's ratio ($\nu = 0.3$) but different α_1 parameters. The first material with $\alpha_1 = 1500$ is stronger in tension than compression while the other material with $\alpha_1 = -1500$ is strong in compression than tension (see Fig. 1 (b)). Fig. 10 (a) and (b) depict the final bridge designs obtained by considering materials with $\alpha_1 = 1500$ and $\alpha_1 = -1500$, respectively, together with their corresponding convergence histories. It is immediate that the two materials with different α_1 parameters lead to bridge designs with distinct layouts. The material with $\alpha_1 = 1500$ is stronger in tension, thus, considering it in the optimization yields a design which resembles a suspension bridge as shown in Fig. 10 (a). On the other hand, the material with $\alpha_1 = -1500$ is stronger in compression, hence, considering it in the optimization leads to an arch bridge-like design as shwon in Fig. 10 (b). In summary, this example demonstrates the effectiveness of the proposed topology optimization formulation in capturing the influence of different material properties in the layout of practical designs.

6. Concluding remarks

In this paper, we introduce an effective topology optimization framework considering hyperelastic materials under small deformations. To account for material nonlinearity, we present a general constitutive model based on the Ogden model under both plane strain and plane stress conditions. By varying the material parameters, the constitutive model captures a wide range of behavior, from tension-dominated (stronger in tension) to compression-dominated (stronger in compression). Moreover, the convexity and strain hardening response of the constitutive model ensure that the nonlinear state equations have a unique solution and that we can confidently use a load control strategy (i.e. the structure has no limit points).

The robustness of the topology optimization framework is reflected in both the optimization formulation and the solution of the nonlinear state equations. In terms of the optimization formulation, we choose the objective function so that we do not need to solve for an adjoint vector in the sensitivity analysis, which leads to improved computational efficiency. Additionally, the sensitivities are always non-positive (a desirable feature). We also adopt two continuation schemes: one continuation for the penalization parameter in the material interpolation; and another continuation to gradually reduce the radius of the density filter at the final stage of the optimization, which is shown to promote closely black and white designs. In terms of solving the nonlinear state equations, the unknown displacement at every given optimization step is always a unique minimizer of the potential energy provided that the tangent modulus tensor remains positive definite. Thus, it is free of global and local instabilities and multiple solutions that may occur when geometrical nonlinearities are included. We further introduce an inexact line search scheme in the standard Newton's method when solving the nonlinear state equations. The inexact line search scheme significantly improves convergence performance in solving the nonlinear system of equations, which is in agreement with previous topology optimization investigations [52]. The robust nonlinear structural analysis allows us to study problems with low volume fractions (e.g. Example 2 of this paper), providing an interesting connection to truss-like structures and truss-layout optimization [2]. We thoroughly study the proposed topology optimization framework through four representative numerical examples, including a practical bridge design example. In all the examples, the objective function always converges smoothly, except for the steps where continuation of penalization factor and/or filter radius are performed (as expected). We also demonstrate that, unlike the standard topology optimization considering linear elastic material, the proposed optimization framework is capable of capturing the influence of nonlinear material behavior, load levels and loading conditions on the layout of optimal structures.

Acknowledgment

The authors acknowledge the financial support from the US National Science Foundation (NSF) under project #1663244, from the Brazilian agency CNPq (National Council for Research and Development), and from the Laboratory of Scientific Computing and Visualization (LCCV) at the Federal University of Alagoas (UFAL). We are also grateful for the endowment provided by the Raymond Allen Jones Chair at the Georgia Institute of Technology. The information provided in this paper is the sole opinion of the authors and does not necessarily reflect the views of the sponsoring agencies.

References

[1] Achtziger W. Truss topology optimization including bar properties different for tension and compression. Struct Optim 1996;12(1):63–74.
[2] Achtziger W. Topology optimization of discrete structures. Vienna: Springer; 1997. p. 57–100.
[3] Allaire G. Shape optimization by the homogenization method. 146. Springer Science & Business Media; 2001.
[4] Allaire G, Francfort G. Existence of minimizers for non-quasiconvex functionals arising in optimal design. Ann Inst Henri Poincare Anal.. vol. 15. Elsevier; 1998. p. 301–39.
[5] Amstutz S, Novotny A, de Souza Neto E. Topological derivative-based topology optimization of structures subject to drucker–prager stress constraints. Comput Methods Appl Mech Eng 2012;233:123–36.
[6] Armijo L. Minimization of functions having Lipschitz continuous first partial derivatives. Pacific J Math 1966;16(1):1–3.
[7] Beer F, DeWolf J, Johnston Jr. ER, Mazurek D. Mechanics of Materials. McGraw-Hill Education; 2014.
[8] Bendsœ MP. Optimal shape design as a material distribution problem. Struct Optim 1989;1(4):193–202.
[9] Bendsœ MP, Sigmund O. Material interpolation schemes in topology optimization. Arch Appl Mech 1999;69(9–10):635–54.
[10] Bertsekas DP, Belmont M. Nonlinear programming. Athena Sci 1999.
[11] Bonet J, Wood RD. Nonlinear continuum mechanics for finite element analysis. Cambridge University Press; 2008.
[12] Bourdin B. Filters in topology optimization. Int J Numer Methods Eng 2001;50(9):2143–58.
[13] Bourdin B, Chambolle A. Design-dependent loads in topology optimization. ESAIM: control. Optim Calc Var 2003;9:19–48.
[14] Bruggi M, Duysinx P. A simplified approach to the topology optimization of structures in case of unilateral material/supports. 10th World Congress on Structural and Multidisciplinary Optimization. 2013. p. 1–9.
[15] Buhl T, Pedersen C, Sigmund O. Stiffness design of geometrically nonlinear structures using topology optimization. Struct Multidiscip Optim 2000;19(2):93–104.
[16] Cai K. A simple approach to find optimal topology of a continuum with tension-only or compression-only material. Struct Multidiscip Optim 2011;43(6):827–35.
[17] Cai K, Cao J, Shi J, Liu L, Qin Q. Optimal layout of multiple bi-modulus materials. Struct Multidiscip Optim 2016;53(4):801–11.
[18] Chi H, Talischi C, Lopez-Pamies O, Paulino GH. Polygonal finite elements for finite elasticity. Int J Numer Methods Eng 2015;101:305–28.
[19] Chi H, Talischi C, Lopez-Pamies O, Paulino GH. A paradigm for higher-order polygonal elements in finite elasticity using a gradient correction scheme. Comput Methods Appl Mech Eng 2016;306:216–51.
[20] Cook RD, et al. Concepts and applications of finite element analysis. John Wiley & Sons; 2007.
[21] Dambrine M, Kateb D. On the ersatz material approximation in level-set methods. ESAIM 2010;16(3):618–34.
[22] Du Z, Zhang W, Zhang Y, Xue R, Guo X. Structural topology optimization involving bi-modulus materials with asymmetric properties in tension and compression. Comput Mech 2018:1–29.
[23] Feng Z, Peyraut F, He Q. Finite deformations of Ogden's materials under impact loading. Int J Non Linear Mech 2006;41(4):575–85.
[24] Guan H, Steven GP, Xie Y. Evolutionary structural optimisation incorporating tension and compression materials. Adv Struct Eng 1999;2(4):273–88.
[25] Haftka R, Kamat M. Simultaneous nonlinear structural analysis and design. Comput Mech 1989;4(6):409–16.
[26] Hughes TJR. The finite element method: linear static and dynamic finite element analysis. Courier Dover Publications; 2012.
[27] Kawamoto A. Stabilization of geometrically nonlinear topology optimization by the levenberg–marquardt method. Struct Multidiscip Optim 2009;37(4):429–33.
[28] Kemmler R, Lipka A, Ramm E. Large deformations and stability in topology optimization. Struct Multidiscip Optim 2005;30(6):459–76.
[29] Klarbring A, Strömberg N. A note on the min-max formulation of stiffness

optimization including non-zero prescribed displacements. Struct Multidiscip Optim 2012;45(1):147–9. 1
[30] Klarbring A, Strömberg N. Topology optimization of hyperelastic bodies including non-zero prescribed displacements. Struct Multidiscip Optim 2013;47(1):37–48.
[31] Liu S, Qiao H. Topology optimization of continuum structures with different tensile and compressive properties in bridge layout design. Struct Multidiscip Optim 2011;43(3):369–80.
[32] Luo Y, Wang MY, Kang Z. Topology optimization of geometrically nonlinear structures based on an additive hyperelasticity technique. Comput Methods Appl Mech Eng 2015;286:422–41.
[33] Ogden R. Large deformation isotropic elasticity-on the correlation of theory and experiment for incompressible rubberlike solids. Proceedings of the Royal Society of London A: Mathematical, Physical and Engineering Sciences. vol. 326. 1972. p. 565–84.
[34] Ogden RW. Nonlinear elastic deformations. Courier Dover Publications; 1997.
[35] Pedersen P. Some general optimal design results using anisotropic, power law nonlinear elasticity. Struct Multidiscip Optim 1998;15(2):73–80.
[36] Querin OM, Victoria M, Martí P. Topology optimization of truss-like continua with different material properties in tension and compression. Struct Multidiscip Optim 2010;42(1):25–32.
[37] Ramos Jr. AS, Paulino GH. Convex topology optimization for hyperelastic trusses based on the ground-structure approach. Struct Multidiscip Optim 2015;51(2):287–304.
[38] Rozvany GIN, Zhou M, Birker T. Generalized shape optimization without homogenization. Struct Optim 1992;4(3–4):250–2.
[39] Sekimoto T, Noguchi H. Homologous topology optimization in large displacement and buckling problems. JSME Int J Ser A 2001;44:616–22.
[40] Sigmund O, Petersson J. Numerical instabilities in topology optimization: a survey on procedures dealing with checkerboards mesh-dependencies and local minima. Struct Multidiscip Optim 1998;16(1):68–75.
[41] Talischi C, Paulino GH, Pereira A, Menezes IFM. Polymesher: a general-purpose mesh generator for polygonal elements written in matlab. Struct Multidiscip Optim 2012;45(3):309–28.
[42] Talischi C, Paulino GH, Pereira A, Menezes IFM. Polytop: a matlab implementation of a general topology optimization framework using unstructured polygonal finite element meshes. Struct Multidiscip Optim 2012;45(3):329–57.
[43] Taylor J. A global extremum principle for the analysis of solids composed of softening material. Int J Solids Struct 1993;30(15):2057–69.
[44] Taylor JE. A global extremum principle in mixed form for equilibrium analysis with elastic/stiffening materials (a generalized minimum potential energy principle). J Appl Mech 1994;61(4):914–8.
[45] Taylor JE, Washabaugh PD. Analysis and design of trussed structures made of elastic/stiffening materials. Struct Optim 1994;8(1):1–8.
[46] van Dijk N, Langelaar M, van Keulen F. Element deformation scaling for robust geometrically nonlinear analyses in topology optimization. Struct Multidiscip Optim 2014;50(4):537–60.
[47] Wachspress EL. A rational finite element basis. New York: Academic Press; 1975.
[48] Wang F, Lazarov BS, Sigmund O, Jensen JS. Interpolation scheme for fictitious domain techniques and topology optimization of finite strain elastic problems. Comput Methods Appl Mech Eng 2014;276:453–72.
[49] Wriggers P. Nonlinear finite element methods. 4. Springer; 2008.
[50] Yoon G, Kim YY. Element connectivity parameterization for topology optimization of geometrically nonlinear structures. Int J Solids Struct 2005;42(7):1983–2009.
[51] Zhang X, Paulino GH, Ramos Jr. AS. Multi-material topology optimization with multiple volume constraints: a general approach applied to ground structures with material nonlinearity. Struct Multidiscip Optim 2017. Accepted
[52] Zhang X, Ramos AS, Paulino GH. Material nonlinear topology optimization using the ground structure method with a discrete filtering scheme. Struct Multidiscip Optim 2017;55(6):2045–72.